



**HAL**  
open science

# Analysis of the effect of the 3C kinematic field of a confined impinging jet on a slotted plate by stereoscopic PIV

Jana Hamdi, Hassan Assoum, Kamel Abed-Meraïm, Anas Sakout

► **To cite this version:**

Jana Hamdi, Hassan Assoum, Kamel Abed-Meraïm, Anas Sakout. Analysis of the effect of the 3C kinematic field of a confined impinging jet on a slotted plate by stereoscopic PIV. *European Journal of Mechanics - B/Fluids*, 2019, 76, pp.243-258. 10.1016/j.euromechflu.2019.02.012 . hal-02447319

**HAL Id: hal-02447319**

**<https://univ-rochelle.hal.science/hal-02447319>**

Submitted on 22 Oct 2021

**HAL** is a multi-disciplinary open access archive for the deposit and dissemination of scientific research documents, whether they are published or not. The documents may come from teaching and research institutions in France or abroad, or from public or private research centers.

L'archive ouverte pluridisciplinaire **HAL**, est destinée au dépôt et à la diffusion de documents scientifiques de niveau recherche, publiés ou non, émanant des établissements d'enseignement et de recherche français ou étrangers, des laboratoires publics ou privés.



Distributed under a Creative Commons Attribution - NonCommercial 4.0 International License

# Analysis of the Effect of the 3C Kinematic Field of a Confined Impinging Jet on a Slotted Plate by Stereoscopic PIV

Jana Hamdi<sup>a,\*</sup>, Hassan Assoum<sup>b</sup>, Kamel Abed-Meraïm<sup>a</sup>, Anas Sakout<sup>a</sup>

<sup>a</sup>LaSIE, University of La Rochelle, Avenue Michel Crépeau, Pôle Sciences et Technologies, 17000 La Rochelle, France

<sup>b</sup>Beirut Arab University-Tripoli Campus, Corniche El Meena, next to the Olympic Stadium, Tripoli, Lebanon

## Abstract

Confined jets impinging on slotted surfaces are usually used in industry, transportation, housing and many other fields. In the construction industry, these jets can be used in ventilation systems to improve the mixing and diffusion of airflows. The terminal devices of these ventilation and air-conditioning systems can, in some cases, become sources of acoustic noise through the self-sustained tones that they can generate. Self-sustained tones occur when a feedback loop settles between the contact area of a jet with a slotted surface and the jet exit. In order to solve this problem, a detailed analysis of the jet must be carried out. The objective of this work was to analyze a flow by studying the effect of the third component of the kinematic field on large-scale structures and energy distribution. This study was performed by comparing the 2C and 3C kinematic fields measured by both PIV and SPIV acquisitions. First, an experimental platform was developed to generate a flow corresponding to the configuration of a confined impinging jet on a slotted plate. Secondly, time resolved particle image velocimetry (TR-PIV) experiments were carried out using both 2D-2C PIV and 2D-3C stereoscopic PIV acquisitions in order to study the influence of the third component. Thirdly, the snapshot proper orthogonal decomposition technique (POD) was applied to both measurements in order to analyse the reveal of the large-scale structures in the jet. The combination of (PIV & SPIV) and POD analysis showed that it is possible to isolate a few typical patterns from the apparently chaotic fluctuations of the jet. Moreover, the time variation of the POD modes was analysed by projecting the time-resolved data series onto the orthonormal basis derived from the POD. The results showed that, for both acquisitions, the first two modes represent the large-scale vortices responsible for the convection phenomenon. The results of the POD modes were similar for both campaigns, with the appearance of an additional mode representing the  $z$  fluctuations. The results also showed that the convergence of the energy of the flow was slower by considering the three components of the velocity field. In fact, for a 2D-3C POD, 198 modes were needed to obtain 90% of the total energy, while 61 modes were sufficient for a 2D-2C POD to obtain the same total energy.

**Keywords** Impinging jet; Stereoscopic PIV; Snapshot POD; Jet Analysis

\*Corresponding author

E-mail address: [jana.hamdi@univ-lr.fr](mailto:jana.hamdi@univ-lr.fr)

## 1. Introduction

Jets impinging upon a solid wall represent an important class of fluid flow configurations. They are of great importance in engineering, particularly in applications for heating, cooling or drying. One of these configurations is the circular impinging jets that were studied by El Hassan ([1] & [2]). A lot of work on impinging jets has been published over the last fifty years. These studies focused on the energy transfer that enables these impinging jets to be used. One of the most important studies is that of Martin [3], who provides a general discussion on the properties of a round jet. Another comprehensive study on the interaction of a flow with an obstacle was performed by Webb and Ma [4]. In this work, the authors present results on energy transfer and velocity field by examining both circular and two-dimensional streams. The roughness of the wall obstructing the flow and the effect of the inclination of the jet were also examined. The first experiments on turbulent planar jets were conducted by Forthmann [5], and the first measurements of turbulence characteristics in circular jets were those of Corrsin [6]. Studies of free jets were continued by researchers such as Rajaratnam [7] and Wygnanski and Fiedle [8]. Many studies have looked at the acoustic loops obtained in plane jets impinging on a slotted plate. The acoustic study of this type of configuration was

detailed by Billon [9] [10], Glesser [11] and Assoum [12] [13] [14]. Billon analyzed the flow instabilities that produce a slot tone and the coupling between the slot tone and acoustic resonances of the flow supply duct. Glesser investigated the aero-acoustic coupling of a jet-slot oscillator to the acoustic resonances of the flow-supply duct. Assoum used another technique to study plane jets impinging on a slotted plate, treating this configuration experimentally using the time-resolved PIV technique, which can be used to measure the 2D velocity vector. He studied the plane dynamic phenomenon and its coupling with the acoustic field [14], as well as the relation of the trajectories of the vortices with the acoustic level [13]. These studies were performed with respect to three parameters: confinement ( $L/H$ ), the Reynolds number ( $Re$ ) and the plate slot [12]. In addition, energy transfer between the acoustic field and the 2D fluctuations was studied for two configurations [15]. Moreover, the correlation between the acoustic field and vortex dynamics was also discussed [16]. From a volumetric point of view, Hamdi et al. [17] elaborated a 3D technique to reconstruct mean velocity fields based on 2D-3C fields using the Proper Orthogonal Decomposition and the phase averaging technique [18].

Generally, any physical problem in any field can be represented by a mathematical model. Modelling gives us a continuous form of the mathematical problem. This problem can be approximated in a numerical model by means of an adequate discretization. The choice of the discretization is primordial in order to reduce the error between the theoretical solution and the numerical solution to a minimum. Indeed, the precision of a numerical model increases with the sensitivity of the discretization, which makes the calculation very expensive for a good approximation of the solutions to complex problems. The high cost has therefore led to a search for model reduction in many areas of science and engineering. Indeed, to be able to reduce a model it is sufficient to project it onto a reduced set of functions with smaller dimensions than the dimensions of the numerical model, giving us a system of equations with very few unknowns. One of the best-known methods is Proper Orthogonal Decomposition (POD), which is designed to find the first dominant eigenvectors of the spatial correlation of the velocity field. So in other words, POD provides an energy-efficient basis for representing a flow. This decomposition method can be used to construct models that capture the key mechanisms of flow dynamics.

In fluid mechanics, POD was introduced by Lumley [19] in order to objectively define coherent structures within turbulent flows. In the same field, POD applications are mainly used as a data processing instrument. Another example of the application of POD in the experimental study of turbulent flows is its use in determining the phase average of particle image velocimetry data, which is of particular interest to us in our study. In the case of laminar or transitional flows [20] [21], POD has proven to be a powerful tool for the identification and dissociation of complex instationnarities induced by the amplification of modes of instability responsible for the transition to turbulence. Although historically implemented as a post-processing tool, POD has more recently been used to construct smaller subspaces for the development of simplified physical models with a low degree of freedom. In this context, POD can be considered as an approximation method.

For flows with a low Reynolds number, the topology of coherent structures is highlighted mainly by visualizations. For turbulent flows, small scales darken the visualization of larger scales, whose contribution to the organization of shear flows is essential. Turbulence is an important topic for scientific research, but it is also one of the least understood [22]. The Navier-Stokes equations are an excellent mathematical model for turbulence. The approximation of this mathematical model lies in a numerical model using appropriate discretization, which makes a small error between the theoretical solution and the numerical solution. One of the major problems is that these equations are not linear and are difficult to solve for a high Reynolds number (that is, for a turbulent jet), even with simple geometries. The accuracy of a digital model increases with the choice of discretization. This makes it difficult to calculate solutions for complex problems with a good approximation.

Proper Orthogonal Decomposition (POD) is designed to find the first dominant eigenvectors of the spatial correlation of the velocity field. Thus, POD provides an optimal energy basis for representing a flow. This decomposition method allows us to build models that capture the key mechanisms of flow dynamics. POD is used in many fields (e.g. fluid mechanics, aerospace and chaotic vibration systems) to build models with

very small dimensions and to approach the solution of the main model, described by partial differential equations.

In fact, the POD technique ([19], [23], and [22]) identifies the highest energy contributions and obtains the spatial structure of the corresponding modes. The basic idea is to describe a given statistical set with the minimum number of deterministic modes. It can be categorized into two basic methods: conventional POD and instant POD (or snapshot POD). Conventional POD was first introduced by Lumley [19] to extract coherent structures from a turbulent flow, while instantaneous POD was suggested by Sirovich [23]. Both approaches are based on the expansion of Karhunen-Loève, in other words these approaches consist in transforming correlated variables into new non-correlated variables. POD has proven to be an effective method for identifying dominant features and events in both experimental and numerical data. It has the added advantage of efficiently compressing or summarizing large amounts of data so that the most useful information about physical processes can be extracted. This method can be used to extract information from the kinematic fields of a flow and is therefore applicable to experimental data (see [24], [25], [26] and [27]). The method determines the highest energy structures by diagonalization of the spatial correlation matrix computed from snapshots. The acknowledged disadvantages in using this method are associated with two issues: (i) energy may not be the right measure to classify the structures of a flow in all cases, and (ii) this decomposition is based on the choice of second-order statistics; thus, valuable phase information may be lost. The first issue has been widely recognized and an explanation for the existence of dynamically highly relevant but energy-free modes was presented by Noack et al [28]. Choosing a set of functions that emphasize the specific structures of a flow can improve the focus on total kinetic disturbance energy. The second issue is more difficult to overcome.

Other methods have been proposed in the literature such as bi-orthogonal decomposition (BOD, see [29] & [30]), which simultaneously produces temporal and spatial structures, called 'Chronos' and 'topos' respectively, via a singular value decomposition of the snapshot matrix. The same result can also be obtained by choosing a temporal or spatial average when calculating the correlation tensor, or by using conventional POD or Snapshot POD, respectively. The temporal structures (chronos) represent the eigenvectors of the temporal correlation matrix in spatial mean, while the spatial structures (topos) constitute the eigenvectors of the temporal mean matrix of spatial correlation. In both cases, the averaging process results in a loss of information that might be important when classifying dynamic processes contained in snapshots. Schmid [31] proposed a decomposition method based solely on flow snapshots, while providing the structures that accurately describe a flow movement. This technique is the basis of Koopman's analysis of non-linear dynamic systems (see [32] & [33]), which has recently been applied to large-scale "cross-jet" simulations by Rowley et al [34].

The control of impinging jets on a slotted plate in order to optimize the aerodynamic, acoustic and thermal comfort necessitate a 3D modelling of the configuration of an impinging jet. Due to the large amount of information present in a 3D flow, a reduced order modelling is to be considered in order to control the flow with a small amount of information. This method is the Proper Orthogonal Decomposition. Our study started at first by analysing the characteristics of a plane impinging jet on a slotted plate at a Reynolds number of  $Re = 4535$  [35], determining the coherent structures by considering 2D PIV measurements. In order to cover all the information, more specifically the aerodynamic phenomena, the objective of this work was to study experimentally the effect of considering the third velocity component on the coherent structures of a confined impinging jet. Snapshot POD was applied to both the 2C and the 3C velocity fields. Energy distribution, spatial modes and changeover time will be discussed and compared.

## **2. Experimental Set up**

### **2.1 The plane impinging jet**

The experimental set up of our study is shown in Figure 1. The airflow was generated by a compressor (1) commanded by a controller (2) that controlled flow velocity. The airflow generated crossed a  $1\text{ m}^3$  settling chamber (3) equipped with three metal grids to ensure an acoustic isolation of the duct from the blower. Afterwards, it passed through a rectangular tube (4)  $1250\text{ mm}$  in length and with a section of  $90 \times 190\text{ mm}^2$ , which was extended by a rectangular convergent (5). Honeycomb sections were inserted into the

rectangular tube to straighten the flow and remove any mean swirl. Hence, the installation creates a free jet  $H = 10 \text{ mm}$  high and  $L_z = 190 \text{ mm}$  wide. The initial velocity at the outlet of the jet ( $U_0 = 7 \text{ m/s}$ ) corresponds to a Mach number of  $M_0 < 1$ . A  $4 \text{ mm}$  thick aluminum plate (6) fitted with a beveled slot (7) was placed parallel to the convergent and was of the same dimensions as the convergent outlet and perfectly aligned with it using a displacement system.

A  $4 \text{ mm}$  thick aluminum plate (6) fitted with a bevelled slot (7) was placed parallel to the convergent, and was of the same dimensions as the convergent outlet. The distance from the exit of the convergent to the impinged plate is denoted by  $L$  and was set at  $40 \text{ mm}$  in this study. Note that confinement is defined as the ratio between  $L$  and  $H$ , i.e.,  $\frac{L}{H} = 4$ . The Reynolds number is calculated as a function of the dimension of the nozzle  $H$  as follows:  $Re = U_0 \cdot H / \nu$ , where  $\nu$  is the kinematic viscosity of the air, and  $U_0$  the initial velocity at the outlet of the jet. In the present configuration, the Reynolds number is equal to  $Re = 4458$  at a temperature of  $23 \text{ }^\circ\text{C}$ .

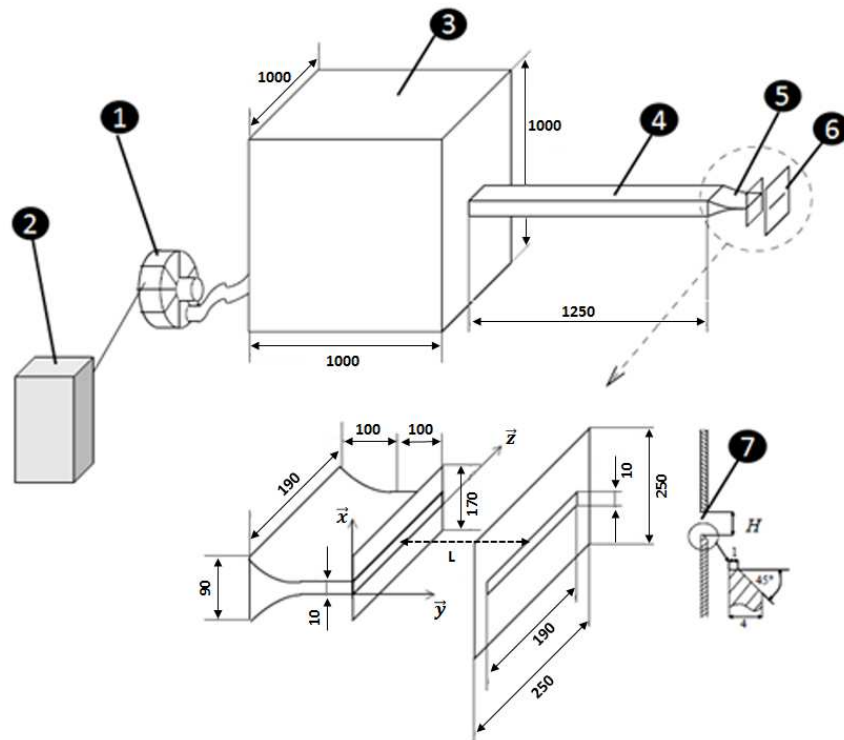


Figure 1: Plane-impinging jet Setup

## 2.2 Stereoscopic-PIV set-up

Two PIV systems were equipped for the present work. The first, presented in Figure 2, was equipped to measure the two velocity components projected onto the laser plane. The second, presented in Figure 3, was equipped to measure the 2D-3C kinematic field of the middle plane.

In the first campaign, two PIV component acquisitions were carried out using a Phantom V711 camera and a double pulsed laser generated by an ND: YLF Litron. Secondly, for the SPIV system, three PIV component acquisitions were carried out, as shown in Figure 3, using two Phantom V711 cameras and a double pulsed laser generated by an ND: YLF Litron.

A 30-mJ energy per pulse and 527 nm wavelength laser was used for both campaigns. This type of high repetition rate laser is used for time-resolved PIV applications. A Laser Guiding Arm is used to offer maximum movability and freedom for transporting laser light from the laser head. This arm is then extended by divergent sheet optics, which generates a 0.5 mm thick plane sheet. The laser beam was fixed across the median plane of the plane jet. The typical time delay between the two pulses was set at  $70 \mu\text{s}$ . The high-resolution cameras were at full resolution at  $1280 \times 800$  Pixels and 7530 Hz frequency. The images were taken at a resolution of  $800 \times 456$  Pixels.

For both campaigns, the cameras were mounted normally to the laser sheet. For stereoscopic configurations, the use of two cameras was necessary in order to have access to the third component of the velocity. The cameras were placed on the same side of the flow to ensure a better depth resolution. In addition, the camera axes were rotated such that the two axes intersected the object plane at the system axis. Furthermore, the object, the lens and the image planes should be collinear so that they satisfy the Scheimpflug condition, which ensures that all particles should be in good focus in the image plane.

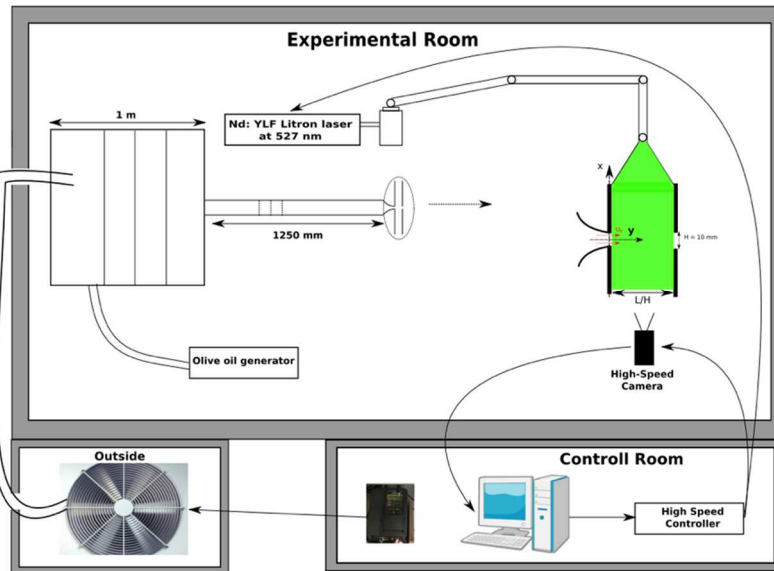


Figure 2: 2D-2C PIV Set-up

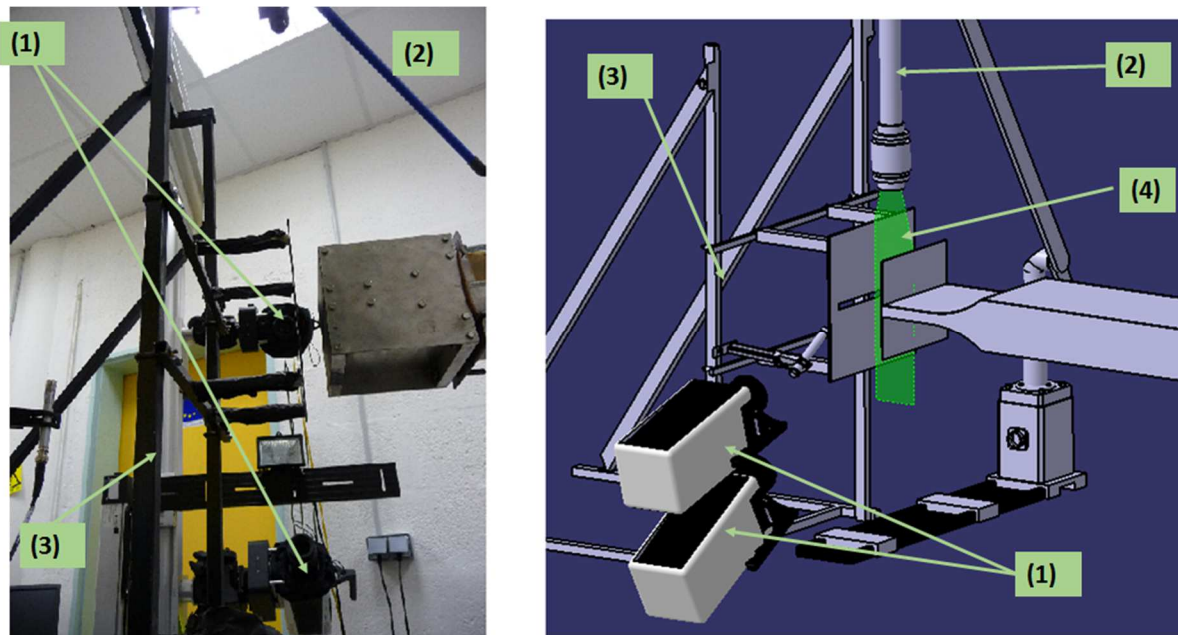


Figure 3: Stereoscopic PIV Set-up

The PIV approach consists in recording two successive and separate images of the flow and applying cross-correlation between them. The interval between the two images can be lowered to  $1 \mu\text{s}$  and, with the use of a pulsed laser, it is easy to study high-speed flows such as the unsteady complex flow occurring in reactive or multi-phase environments. Furthermore, this small interval yields a very small displacement, leading to a reduction of out-of-pattern motion as well as a reduction in the perpendicular velocity component effect. All of these advantages make cross-correlation PIV a very suitable method for resolving the structure of high-speed flows and three-dimensional flows such as those found in an annular jet. The pulsed laser light is chopped by a shutter with a frequency response of up to 10 kHz. This shutter can be triggered by a TTL

signal and is synchronized with the camera using a HSC (High-speed controller) with a time resolution of 10 ns. In the signal diagram shown in Figure 4, the image pairs consist of the first and second frames and the third and fourth... An image pair acquisition rate of 2.5 KHz was used to allow time-resolved sampling of the shedding phenomenon.

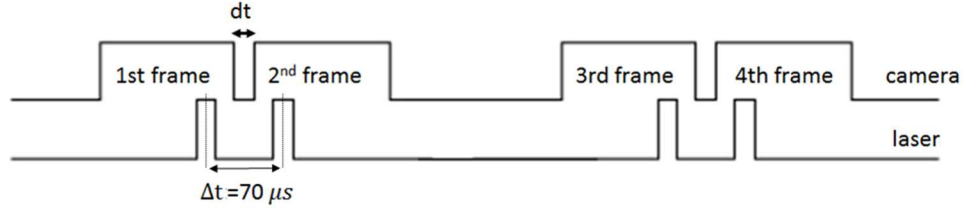


Figure 4: Signal diagram to synchronize camera and laser shutter

Moreover, flow seeding is one of the most important aspects of PIV measurements. The intake air is seeded with droplets of olive oil 2–3  $\mu\text{m}$  in diameter. These were generated in an atomizer by passing air through a bath of olive oil. Both campaigns were acquired at a sampling frequency of 5 KHz, i.e. 2500 doublets of images were taken over an acquisition time of 0.5 s. Note that the pulsation time of the laser was 150 ns. An image pair acquisition rate of 5 KHz was used to allow time-resolved sampling of the shedding phenomenon. Data acquisition and post-processing were performed with Davis 8.3.0 software. The images were processed by an adaptive multi-grid algorithm correlation. During the processing of the PIV images, an interrogation window of  $32 \times 32$  pixels was selected. The average displacement for the particle pairs in each window was calculated using a cross correlation algorithm and was overlapped by 75%, leading to a vector spacing of 70.5 Pixels, which represents a spatial resolution of 0.81 mm. The average size of the particle image was  $2.5 \times 2.5$  pixels, which is an adequate resolution according to Prasad [36].

### 3. Proper orthogonal decomposition

POD is a technique that is at the intersection of various approaches to turbulence. It is based on the statistical processing of a signal, from which a certain coherence or organization is extracted, making it possible to characterize the dynamics of the signal and to predict how it will change with time. It is used in many fields (fluid techniques, aeronautics, vibrations and chaotic systems) to build models with very small dimensions, to approximate the solution of the main model, described by equations to partial derivatives. The objective of POD is to extract an orthogonal and ordered basis, defined as the modal basis or spatial POD basis, in order to identify the most representative degrees of freedom to construct a reduced model of the signal  $u(x, t)$ . In this context, an approximation of the spatio-temporal random process  $u(x, t)$  is sought in the following form:

$$u(x, t) \approx \sum_{i=0}^N a_i(t) \varphi_i(x) \quad (1)$$

where  $a_i(t) = \langle u, \varphi_i(x) \rangle$ .

#### **Direct Method:**

In order to ensure the optimality of this modal basis, POD consists in finding orthogonal modes  $\varphi_i \in H = \text{Hilbert space}$  that minimize the following quadratic error of representation:

$$\frac{1}{T} \int_0^T \left\| u - \sum_{i=1}^N a_i(t) \varphi_i(x) \right\|^2 dt \quad (2)$$

The principal of the POD method is as follows: for  $u(x, t)$  existing in a Hilbert space  $H$  with  $\langle \cdot, \cdot \rangle_H$  as the scalar product,  $\| \cdot \|_H$  the induced norm and a mean operator over  $T$ , the POD modes can be obtained as successive solutions to the constrained optimization problem:

$$\min_{\psi \in H \setminus \{0\}} \frac{1}{T} \int_0^T \left| \langle u - \prod_i u, \psi \rangle \right|^2 dt \quad (3)$$

with:  $\langle \psi, \psi \rangle = \|\psi\|^2 = 1$ .

$\prod_i$  = Orthogonal projection on the subspaces constituted by the  $i^{\text{th}}$  first modes  $\{\varphi_1, \dots, \varphi_i\}$  for  $i \geq 1$ .

Indeed, this method relies on looking for the deterministic modes, which are best correlated with the discrete realizations of the random variable  $u(x, t)$  on average. Thus, the first mode is the one that ensures the best projection of this process; the second is the one that ensures the best projection of the results of this variable orthogonally to the first mode and so on.

Conventionally, the first POD mode can be sought as a solution to the following optimization problem:

$$\max_{\varphi \in H \setminus \{0_H\}} \frac{\frac{1}{T} \int_0^T |\langle \varphi, u(t) \rangle|^2 dt}{\|\varphi\|^2} \quad (4)$$

with  $\langle \varphi, \varphi \rangle = \|\varphi\|^2 = 1$ .

This formulation leads to a maximization of the projection of  $u$  onto the vector line having the same direction of  $\varphi$  on average on  $T$ .

In order to show that this problem is equivalent to a problem with eigenvalues, we introduce the linear operator  $K: H \rightarrow H$  defined by:

$$K\varphi := \frac{1}{T} \int_0^T \langle \varphi, u(t) \rangle u(t) dt. \quad (5)$$

The operator  $K$  is a Hilbert-Schmidt operator (therefore compact and self-adjoint operator). In addition, let  $J(\varphi) := \frac{1}{T} \int_0^T |\langle \varphi, u(t) \rangle|^2 dt$ .

Since the mean operator and the scalar product on  $H$  ( $D$ ) are commutative, it follows that  $J(\varphi) = \langle \varphi, K\varphi \rangle$ . A standard formulation equivalent to problem (4) consists in maximizing the quantity:

$$F(\varphi) = \frac{J(\varphi)}{\langle \varphi, \varphi \rangle} \text{ avec } \varphi \in H \setminus \{0_H\} \quad (6)$$

In the same context, we calculate  $F(\varphi + \psi)$  which is equal to:

$$F(\varphi) + \frac{2 R\langle \psi, K\varphi \rangle_H}{\langle \varphi, \varphi \rangle_H} - 2 F(\varphi) \frac{R\langle \psi, \varphi \rangle_H}{\langle \varphi, \varphi \rangle_H} + \theta(\|\psi\|^2) \quad (7)$$

with  $\psi \in B(0, \epsilon)$  where  $0 < \epsilon \ll 1$  &  $\epsilon < \|\varphi\|$ .

A necessary condition of optimality is the cancellation of the derivative of  $F$ , so if  $\varphi$  is a maximum of (4) then  $\forall \psi \in B(0, \epsilon), R\langle \psi, K\varphi \rangle = F(\varphi) R\langle \psi, \varphi \rangle$ . By repeating the same procedure for  $i\psi$  we obtain  $Im\langle \psi, K\varphi \rangle = F(\varphi) Im\langle \psi, \varphi \rangle$ . This implies that  $\varphi$  is a solution to  $K\varphi = \lambda\varphi, \forall \psi \in B(0, \epsilon)$ .

Conversely, since the operator  $K$  is symmetric and positive, being Hilbert-Schmidt, then the spectral theory implies that the equation  $K\varphi = \lambda\varphi$  has a countable infinity of solutions. The eigenvalues associated with the eigenfunctions of the operator  $K$  are real positive or zero, ordered as:  $\lambda_1 \geq \lambda_2 \geq \lambda_3 \geq \dots \geq \lambda_n \geq \dots \geq 0$ . Every eigenvector  $\varphi$  corresponding to the largest eigenvalue  $\lambda_1$  of  $K$  satisfies (5), so our problem is a problem of eigenvalues. We then deduce the existence of a complete orthonormal basis  $\{\varphi\}_{k=1}^{+\infty}$  such that for all  $u \in H$  we have:  $u = \sum_{i=1}^{+\infty} \langle u, \varphi_i \rangle \varphi_i$ .

The conventional approach of POD is to solve a problem with eigenvalues involving spatial correlations. Its Eigen functions are the spatial POD modes and the temporal coefficients are obtained by projection of  $u$  onto these modes.

### **Snapshot Method:**

The *Snapshot POD* approach consists in first solving an eigenvalue problem on the temporal correlations to determine the temporal coefficients, and then projecting the quantity  $u$  onto these temporal coefficients and deducing the spatial POD modes.

In other words, this method consists in no longer directly looking for the base composed of  $\varphi_i$ , with  $i = 1, \dots, N$  but writing each eigenvector of the operator  $K$  as a linear combination of the fields  $u(x, t_j)$  such that:  $\varphi_i = \sum_{j=1}^{N_t} a_i(t_j)u(x, t_j)$  where  $N_t$  is the number of time samples. So the goal is to look for the coefficients  $a_i(t_j), \forall j = 1, \dots, N_t$  which are acquired by the substitution of  $\varphi_i$  in  $K\varphi = \lambda \varphi$  for all  $j = 1, \dots, N_t$ . The calculation gives us the following expression:

$$R_{jk} \cdot a_i(t_k) = \lambda_i a_i(t_k), \forall k = 1, \dots, N_t \quad (8)$$

where  $R_{jk} = \frac{1}{N_t} \int_{\Omega} u(t_j, x)u(t_k, x) dx$ , and  $\lambda_i$  is the Eigen Value associated with the POD mode  $\varphi_i$ .

## **4. Results and Discussions**

In a previous study [17] we developed a 3D technique for the study of a 3D kinematic field by examining 2D-3C measurements. This technique was developed by taking SPIV measurements of thirty parallel planes. The aim of this work was to study the effect of the third component of the velocity vector on both the analysis of the flow as well as the reconstruction.

This section will be divided into three parts. We will start by presenting some features of a jet flow, particularly the 3C kinematic fields as well as the change in the third component  $V_z$ . In the second part, a detailed comparison will be made between a 2D-2C POD snapshot and a 2D-3C POD snapshot by comparing the spatial modes, how they vary with time and the energy convergence.

### **4.1 General characteristic features of the jet flow**

PIV calculations based on a cross-correlation between the two frames of the instantaneous particle fields gave us the instantaneous kinematic fields. An example of an instantaneous PIV vector field at an arbitrary time is shown in Figure 5, which presents the transversal velocity contour  $V_x$ , the longitudinal velocity contours  $V_y$  together with the vector field and the horizontal transverse contour  $V_z$ . In fact, the slot of the plate corresponds on each of the images of Figure 5 to  $y/H = 4$ , whereas the flow starts at  $y/H = 0$  and  $-0.5 < \frac{x}{H} < 0.5$  and follow the longitudinal component as its direction. Figure 5 shows that for  $V_x$  a vortex appeared on either side of the jet axis, one of positive magnitude and one of negative magnitude, specifically on the axes of the edges of the slotted plate at  $\frac{x}{H} = \pm 0.5$ . On the other side,  $V_y$  shows that the longitudinal velocity was centred on the jet axis and represents the training of the flow. Moreover, a high amplitude of the longitudinal velocity is remarked on the jet axis, synchronized with the appearance of vortices. No specific features were detected relative to the third component velocity. In fact, as shown in Figure 5,  $V_z$  represents small structures on the plate that were due to swirling detachment.

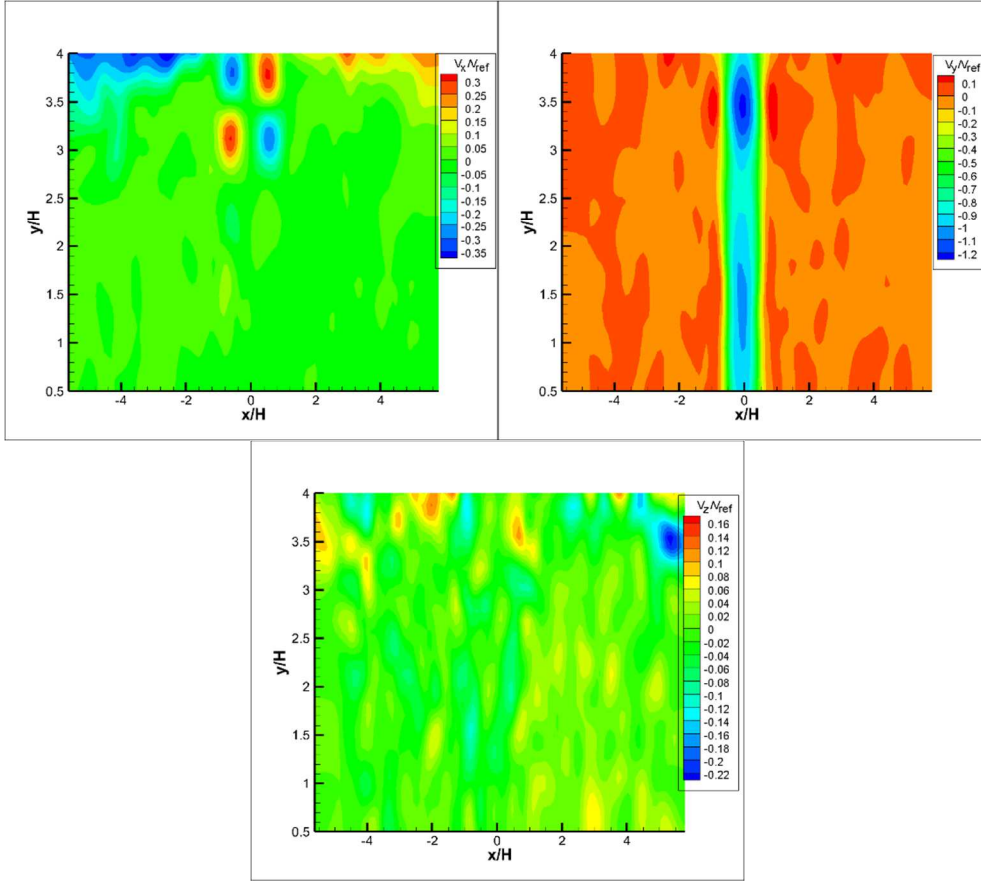


Figure 5: An instantaneous 3C kinematic field ( $V_x, V_y, V_z$ )

Lots of parameters can be studied from these PIV kinematic fields, such as the mean flow and the fluctuating flow. The mean velocity was obtained by averaging the 2500 kinematic instantaneous fields. In order to obtain dimensionless velocities, it was necessary to divide them by a velocity of reference, which we chose to be the free field stream wise velocity. The latter was taken at a place where the uncertainties of PIV measurements were very small. Hence, we took a point in the centre of the potential core and away from the plate. For all velocity profiles presented here,  $V_{ref} = V_{(x/H = -0.8, y/H = 1)}$  which was equal to 7m/s. The mean velocity components are defined as  $\bar{V}_x, \bar{V}_y, \bar{V}_z$ .

To characterize the turbulent flow field, the velocity fluctuations are also calculated. The turbulence rates are defined as the quadratic averages represented by  $\|V'_x\|_{L^2}, \|V'_y\|_{L^2}$  &  $\|V'_z\|_{L^2}$  respectively. Note that  $V'_x = V_x - \bar{V}_x$  represents the fluctuation of the transverse velocity,  $V'_y = V_y - \bar{V}_y$  the fluctuating part of the longitudinal velocity and  $V'_z = V_z - \bar{V}_z$  the fluctuation of the lateral velocity. In addition, the norm  $L_2$  is defined as follows:  $\|V\|_{L^2} = \sqrt{\sum_{i=1}^M V^2(x_i)}$ .

In order to study the third component of the velocity obtained through the stereo-PIV technique, the different profiles of the transverse horizontal velocity  $V_z$  are discussed. First, the profile of the mean transverse velocity  $\bar{V}_z$  was studied at different distances from the plate ( $y/H = 1, 2$  and  $3$ ) on the jet axis for  $x/H = -0.08$ . In addition, two other positions corresponding to the vortex transition were also chosen ( $x/H = -0.62$  and  $x/H = 0.46$ ). The locations of the studied values are presented on Figure 6.

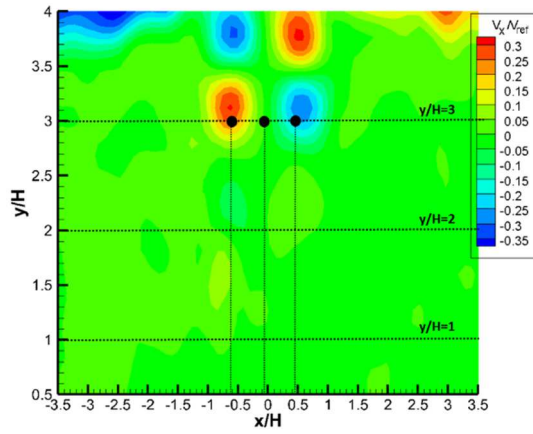


Figure 6: Important Locations

The results shown on Figure 7 indicate that for any distance from the plate,  $\bar{V}_z$  is quasi-null on the jet axis. Near the extremities of the plate, i.e., for  $z > 85 \text{ mm}$  there was a slight increase due to edge effects. Furthermore, the results on the axis of passage of vortices validate the assumption that the lateral mean velocity was quasi-null. For  $x/H = -0.62$  and  $x/H = 0.46$  the change in this parameter was less ordered, while it was always around 0 in the normalized value. Note that for  $x/H = -0.62$  and from the  $P_{60}$  plane, an increase in the value of  $\bar{V}_z$  of up to about 5% was recorded. This horizontal transversal component was negligible compared to the other components. Indeed, on all the measurement points the results were close to zero and remained within the limits of the measurement error.

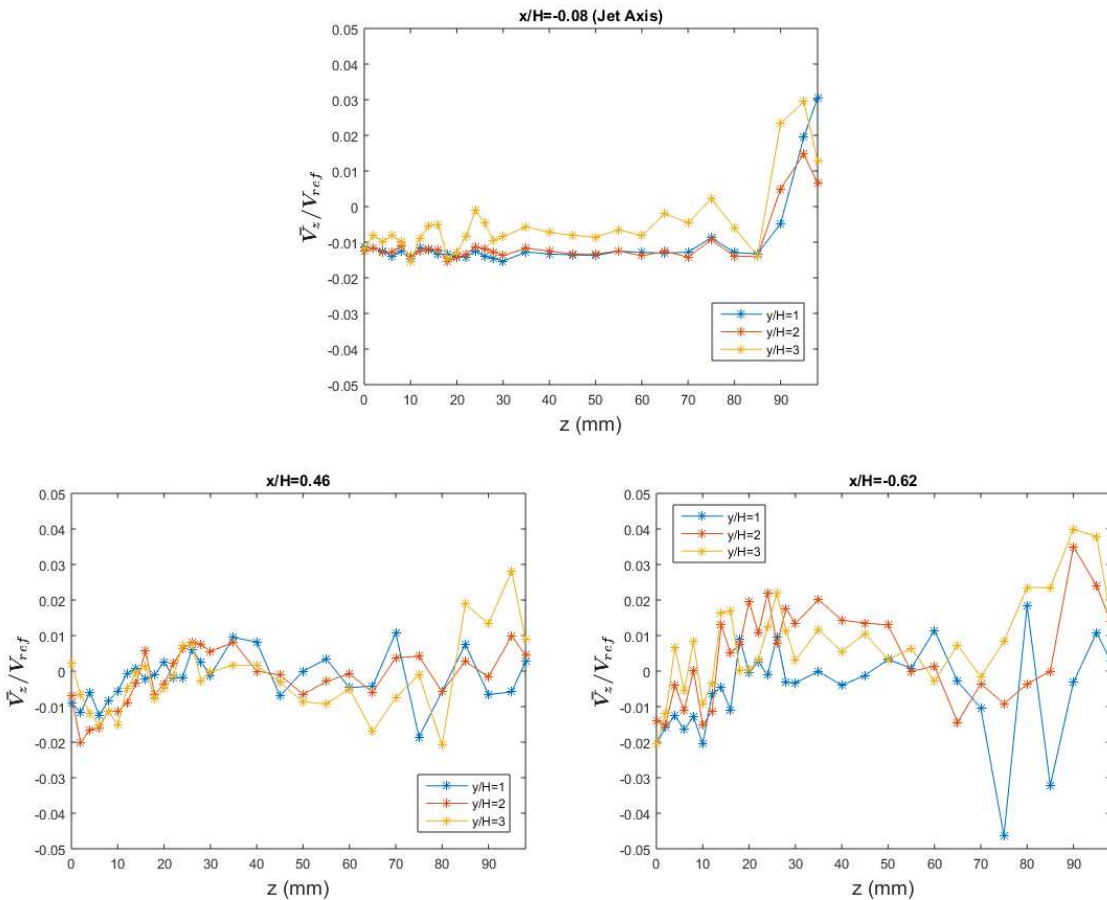


Figure 7: Mean profile of lateral velocity  $\bar{V}_z$

Similarly, the turbulence rate of the third velocity component was studied. Figure 8 shows that this component was of the order of 2 to 3% on the axis of the jet corresponding to  $\frac{x}{H} = -0.08$ . A sharp increase of up to 5% was recorded for  $z > 90$  mm. On the other hand, for the  $x/H = 0.46$  and  $x/H = -0.62$  vortex flow axes, the values for this parameter were not the same. In fact, the turbulence rate close to the jet outlet (i.e. for  $y/H = 1$ ) was of the order of 3% for all recorded planes. Closer to the plate, it was equal to 5% for  $y/H = 2$  and 3 up to plane  $P_{60}$ . From plane  $P_{60}$  the transverse turbulence rate increased close to the plate for  $y/H = 3$  until it reached a value of 12%, due to the effects of the plate edge.

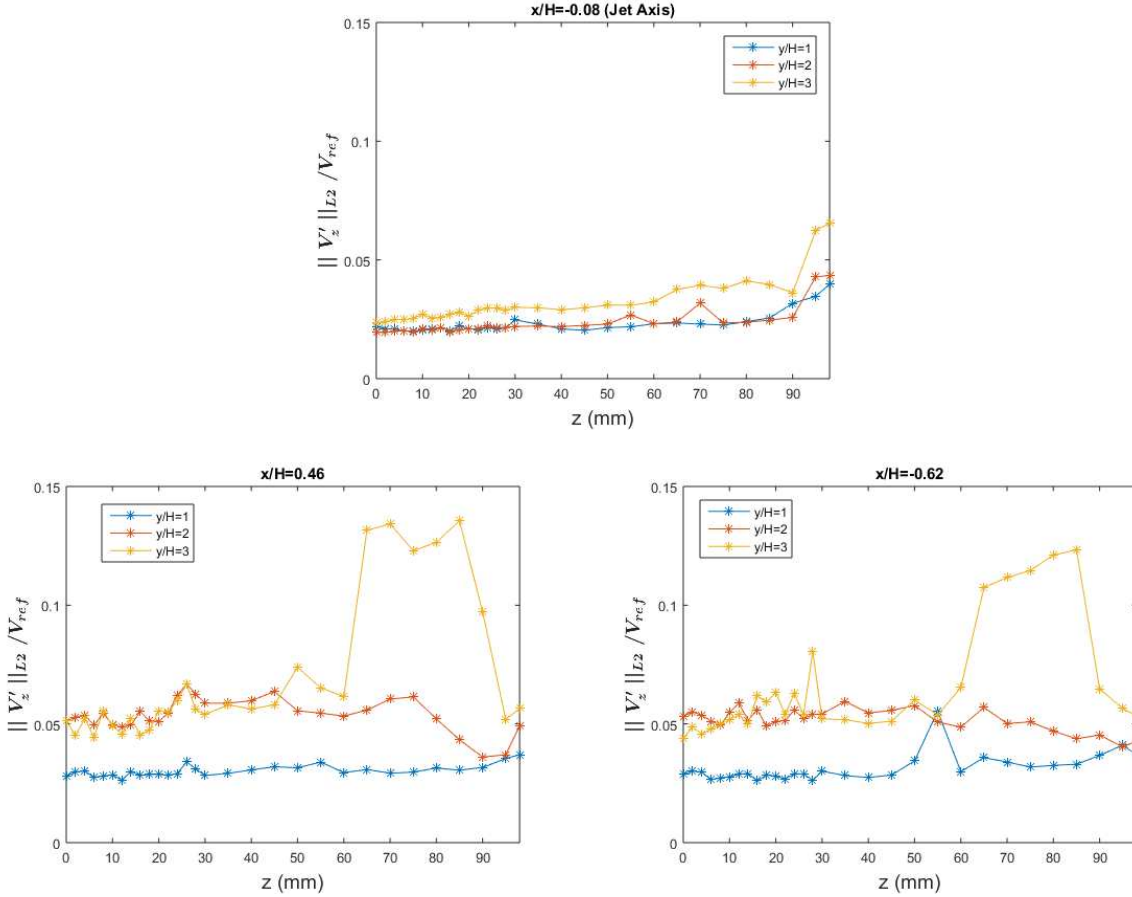


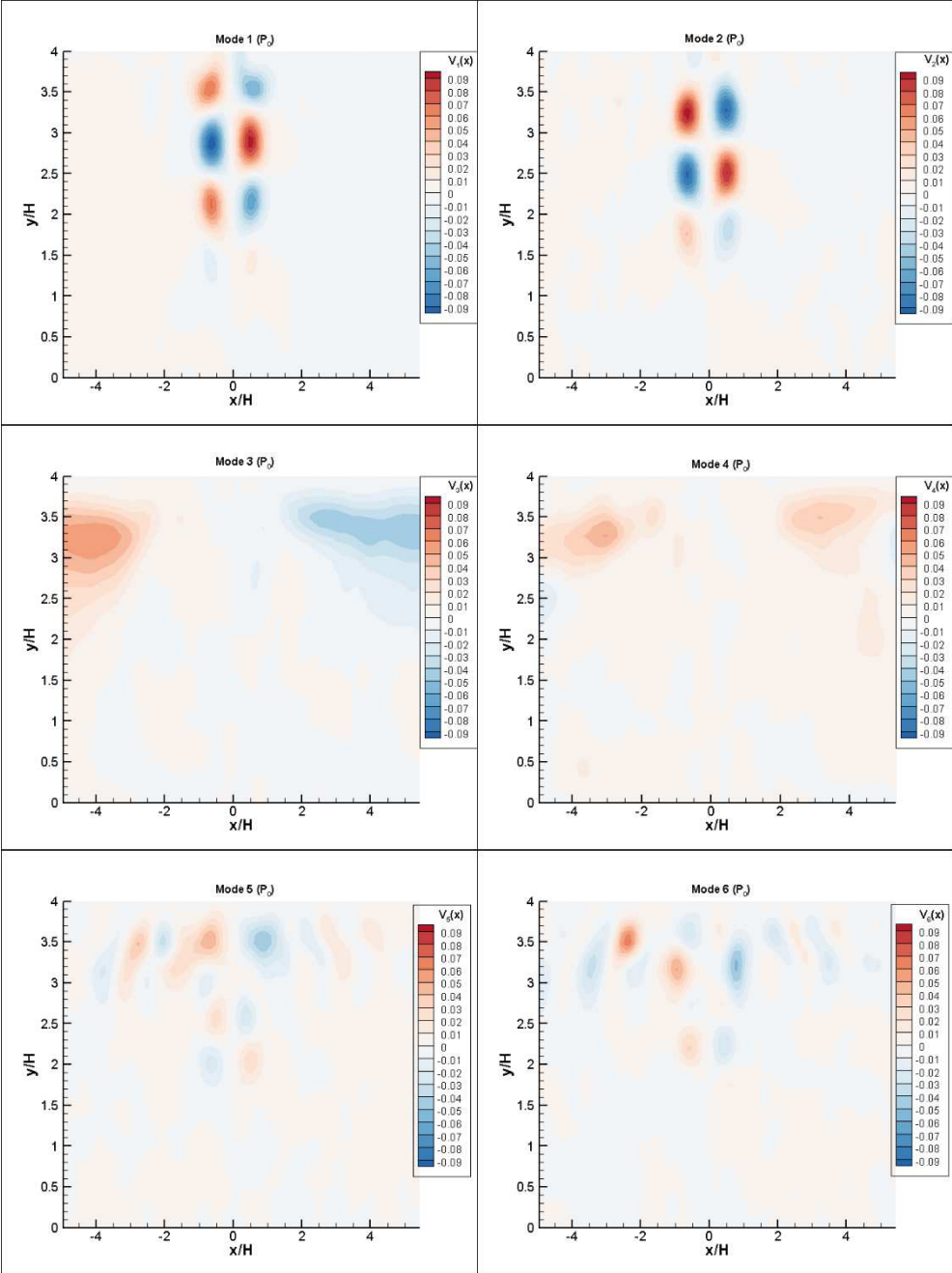
Figure 8: Profile of the lateral fluctuations

## 4.2 Coherent structures

After starting with a 2D-2C POD analysis of the coherent structures present in the 2D PIV measurements [35], we were interested in performing a 2D-3C POD analysis taking into account the third velocity component. From previous work [17], it had been noticed that parallel planes have the same topology as coherent structures. For this reason, the discussion in this section will be centred on one case, the median plane  $P_0$  ( $z = 0$  mm).

A previous study on spatial modes was carried out by building the correlation matrix with the two components of velocity,  $V_x$  and  $V_y$ . It should be noted that the acquisitions in the present work were measured using the SPIV technique. This method gives access to the third component of velocity  $V_z$ , which will therefore be considered in the calculation of the correlation tensor.

4.2.1 Spatial Modes



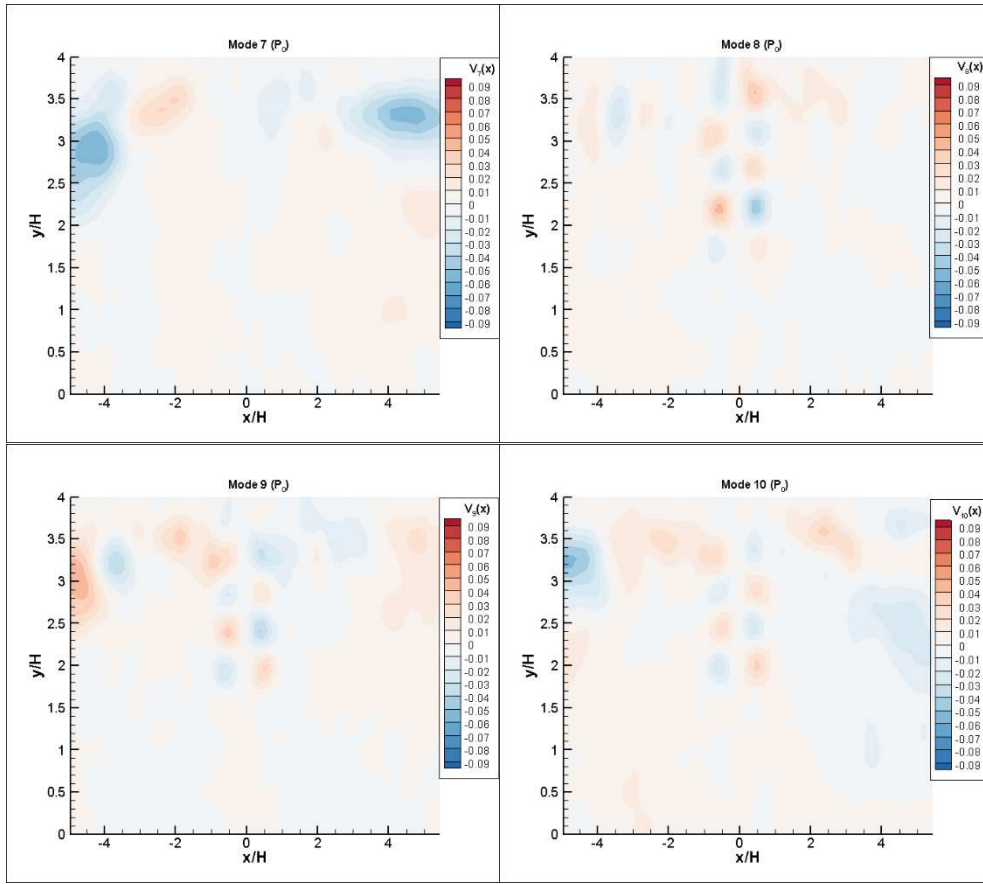
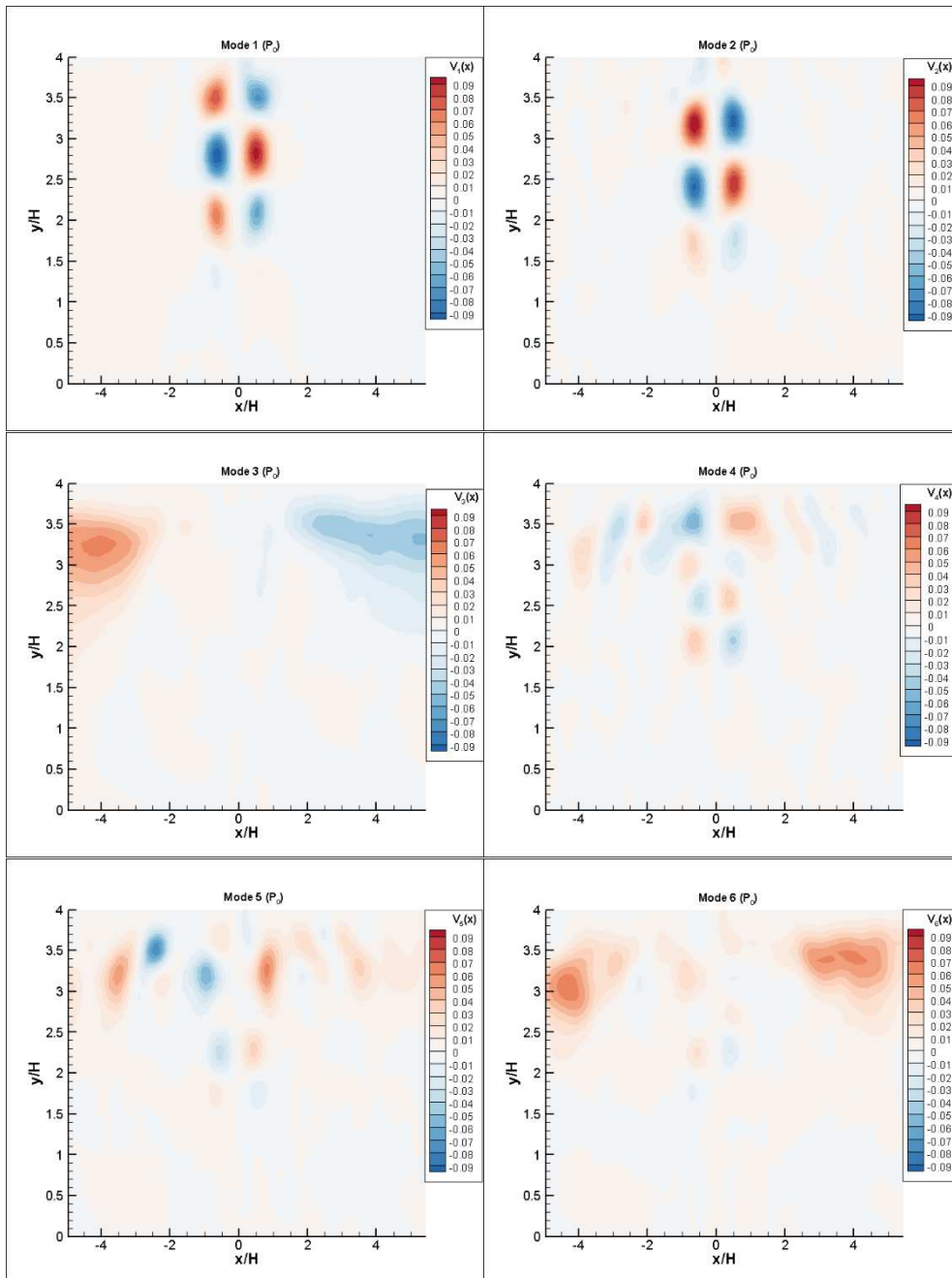


Figure 9: First ten spatial modes  $\Phi_u$  obtained by snapshot POD (2D-3C)

First, the influence of the third component of the velocity on POD was studied by examining the organization of the first ten Eigen modes. The organization of the modes of this decomposition is presented in Figure 9. Comparing these results with those of the 2D-2C decomposition (Figure 10), it can be seen that the first transversal modes were identical between the two decompositions. The first two modes were very similar to those in the 2D-2C decomposition. These modes describe the swirling passage on both sides of the jet axis for  $x/H = \pm 0.5$ , starting from  $y = -17$  mm to a position close to the plate. This result shows that the third component does not influence the flow at this point. Mode 3 is the same as 2D-2C and represents shear at the plate.

On the other hand, the modes in a 2D-3C analysis from mode four are shifted by one mode in comparison to the 2C decomposition. In fact, modes 5, 6 and 7 in the 2D-3C POD were similar to modes 4, 5 and 6 in the 2D-2C POD. Note that mode 4 in 2D-3C POD also gave small swirling scales, especially at the plate.



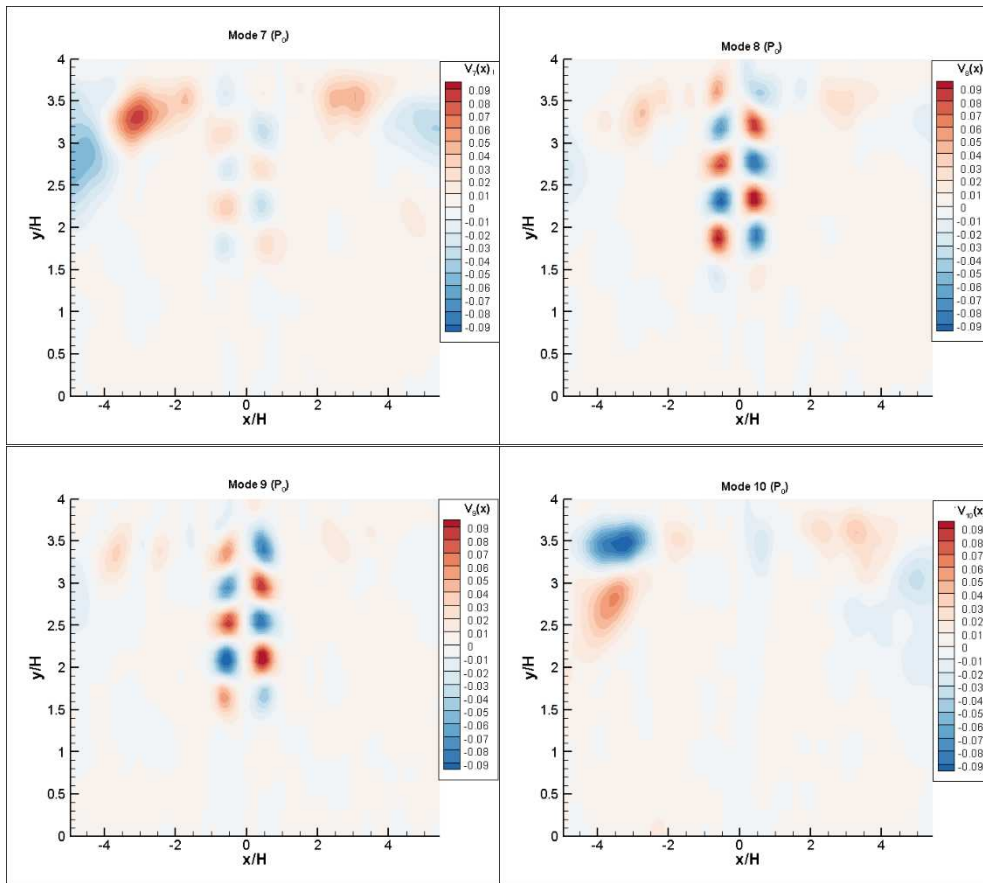
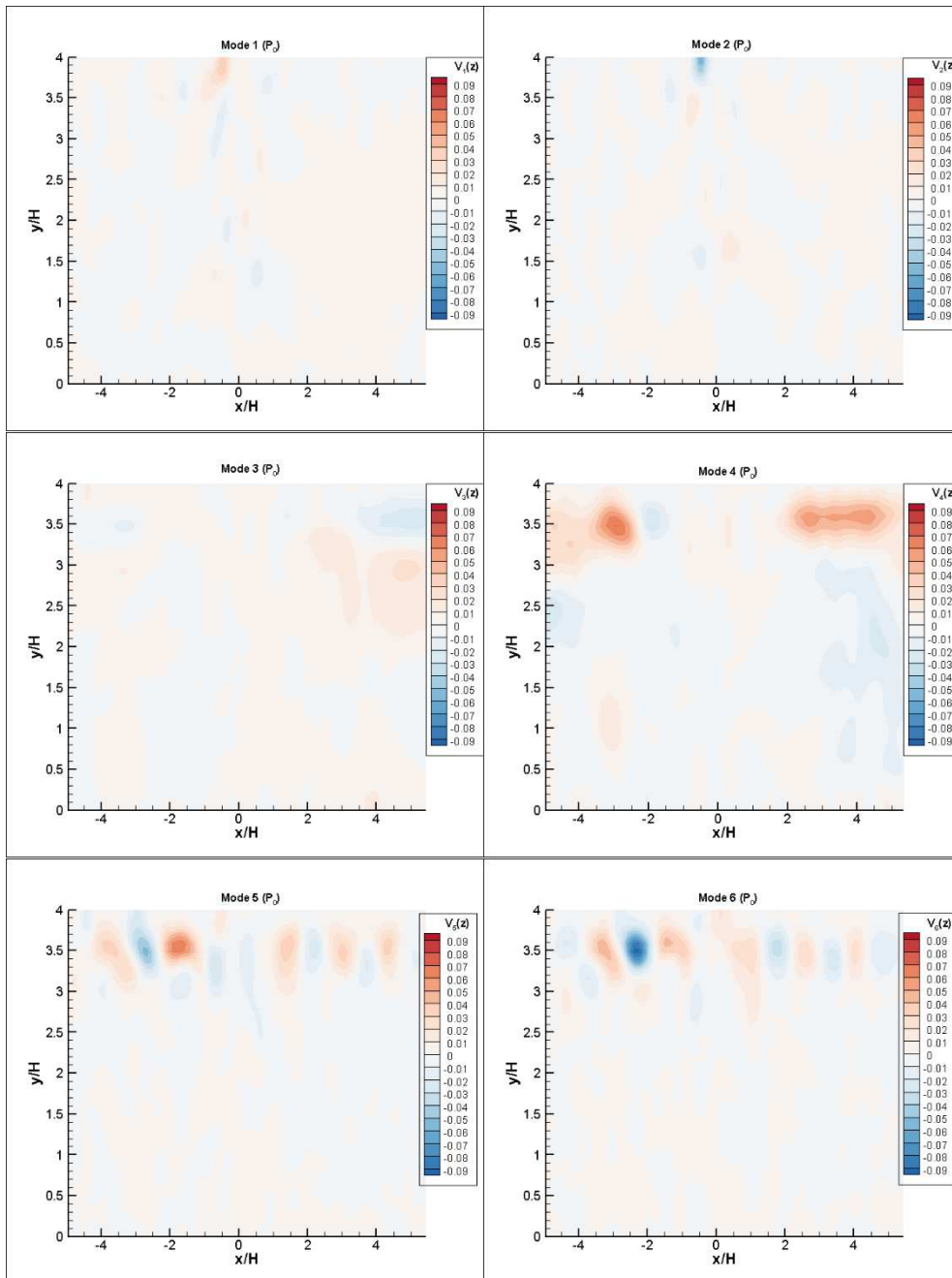


Figure 10: First ten spatial modes  $\Phi_u$  obtained by snapshot POD (2D-2C)

For a deeper understanding of the of the vortex phenomenon in the third direction it was necessary to analyse also the lateral component of the Eigen modes. As seen in Figure 11, which represents the first ten spatial modes  $\Phi_w$  obtained by a 2D-3C POD of the plane  $P_0$ , only the first pair of modes had significant phenomena regarding the creation of vortices. The results show that, along the jet axis, large swirl structures were present which can be considered as swirling rolls that extend throughout the  $z$  direction.



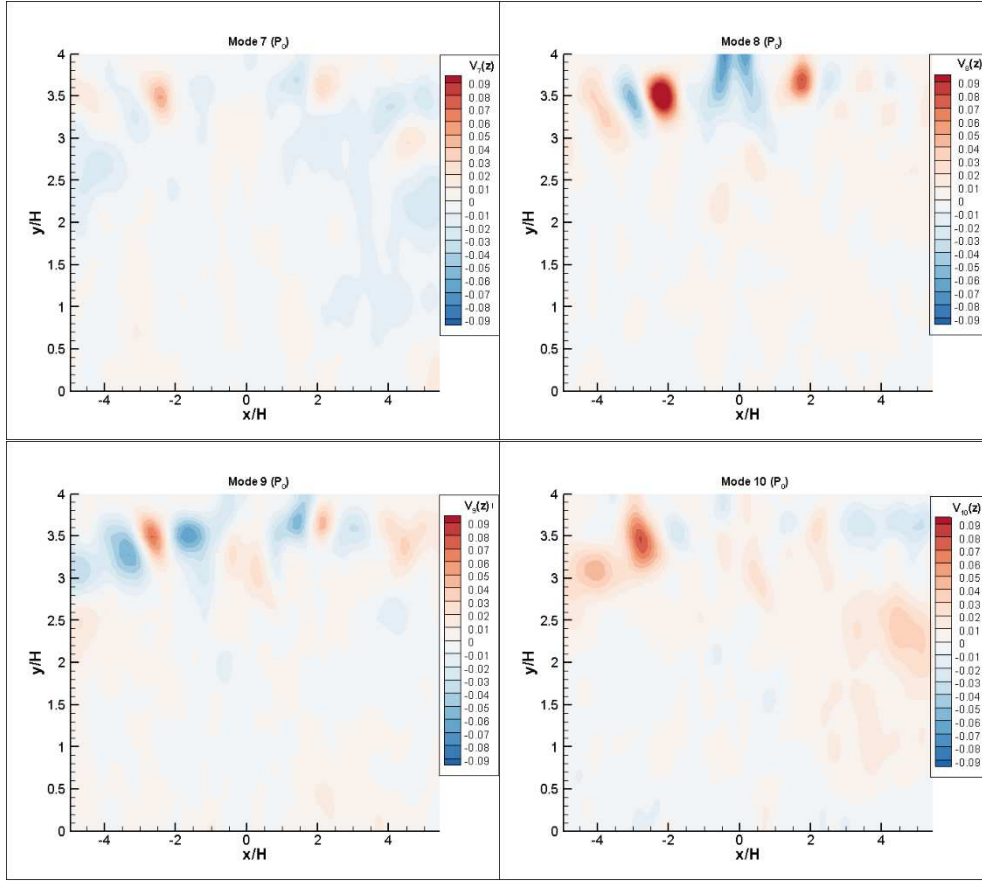


Figure 11: First ten spatial modes  $\Phi_w$  obtained by snapshot POD (2D-3C)

#### 4.2.2 Energy Convergence

A second comparison was made between the eigenvalues of the POD decomposition and the energy it delivers. In fact, the eigenvalue  $\lambda^{(k)}$  divided by the total energy  $E_t$  represents the turbulent kinetic energy  $E_k$  contained in the  $k^{\text{th}}$  mode as follows:

$$E_k = \frac{\lambda^{(k)}}{E_t}, \text{ with } E_t = \sum_{k=1}^N \lambda^{(k)}. \quad (9)$$

Thus, the amount of kinetic energy of the velocity field in Snapshots for a given mode is proportional to the corresponding eigenvalue. Table 1 represents some energy convergence values for the two POD problems (POD2D-2C and POD2D-3C). It was then observed that the convergence of the eigenvalues resulting from the Snapshot POD taking into account the third velocity component was slower than that with two velocity components. In fact, for a POD 2D-3C we needed 198 modes to cover 90% of the total energy, while for a POD 2D-2C only 61 modes were needed to cover the same energy value.

The choice of values of  $N_{(pod)}$  for the convergence of the eigenvalues was essentially related to the energy represented by each mode. The objective of the eigenvalue convergence study was to determine the number of modes required to obtain a cumulative energy of 90%. As already explained, the best reconstruction criterion is to take a mode that cumulates more than 90% of the total energy and the considered mode should have an energy greater than 1%.

In addition, an analysis of the energy delivered by the first two modes is important if, for the fluctuating field, two modes are the most representative of the fluctuations. Table 1 shows that for a 2D-3C POD the first two modes represent 39% of the total energy whereas for a POD 2D-2C the energy value of these two components was much greater. Then, the second choice was  $N_{pod} = 10$  because mode 11 (of the 2D POD -

2C) represents 0.90% of the energy, which is of minimal importance. The third choice was  $N_{pod} = 61$  because mode 62 represents 0.0936% of the energy (2D POD 2C)

$N_{POD}$	POD 2D-2C	POD 2D-3C
2	55.079	39.249
10	76.670	57.926
61	90.415	77.368
198	96.292	90.001
306	97.791	93.7900
486	99.001	96.890
817	99.778	99.001

Table 1: Some values of convergence of the Eigen Values between a POD 2D-2D and a POD 2d-3C

### 4.2.3 Temporal Coefficients

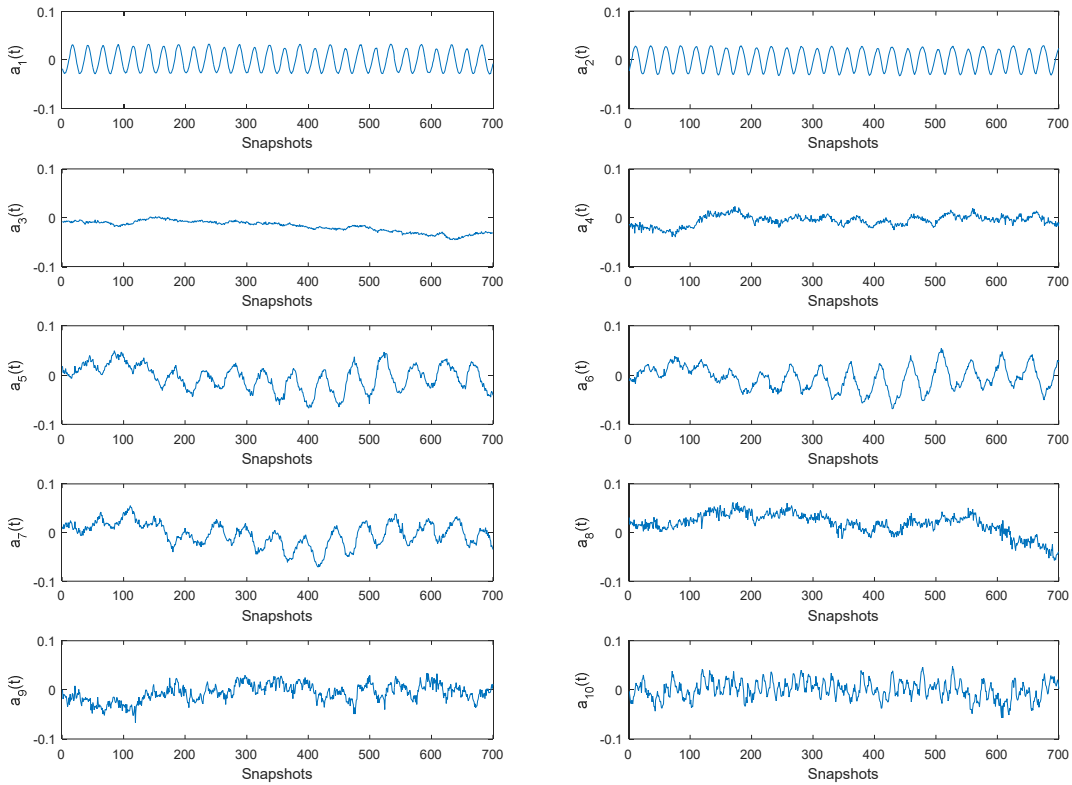


Figure 12: Temporal Evolution of the first ten modes  $a_n(t)$  for a POD 2D-3C

The coefficients  $a_n(t)$  resulting from a decomposition in Eigen modes made it possible to activate the different modes at different points in time for the coherent structures, whose topology is given by the eigenvectors  $\Phi^k(X)$ . For our acquisitions, based on the time-resolved acquisition of the kinematic fields measured by SPIV, the coefficients  $a_n(t)$  were resolved temporally, which allowed us to determine how the modes interacted with each other. This section will analyse this parameter for the two decompositions applied to our measurements.

Figure 12 & Figure 13 present the change over time of the  $a_n(t)$  coefficients for the first ten modes of the POD 2D-3C and POD 2D-2C Snapshot, respectively. These temporally resolved signals were plotted over 750 Snapshots, providing sufficient values for discussion (statistical convergence). The statistical convergence of the flow was 500 Snapshots [33].

It was observed that the first two modes were identical for the two applications (2D-2C and 2D-3C). This means that the third component of velocity does not change anything at the planar vortex flow in the POD problem. There was a quasi-constant decrease of the order of 0.02 in the third mode in both cases. On the other hand, the visualization of the temporal coefficients showed that modes 4 and 5 obtained by POD 2D-2C were similar to the coefficients of modes 5 and 6 of the POD 2D-3C, both having a quasi-sinusoidal form. Note that modes 4 and 5 began close to zero and then after 250 Snapshots the signal had a quasi-sinusoidal form. Finally, modes 8 and 9 for the 2D-2C POD had a quasi-sinusoidal appearance with an envelope of maximum amplitude equal to that of mode 1. In contrast, the signal for these two modes was less clear for the POD 2D-3C, with a more complicated sinusoid. The couples already mentioned seemed to be correlated with each other since they had the same pace and amplitude, i.e. represented the same phenomenon.

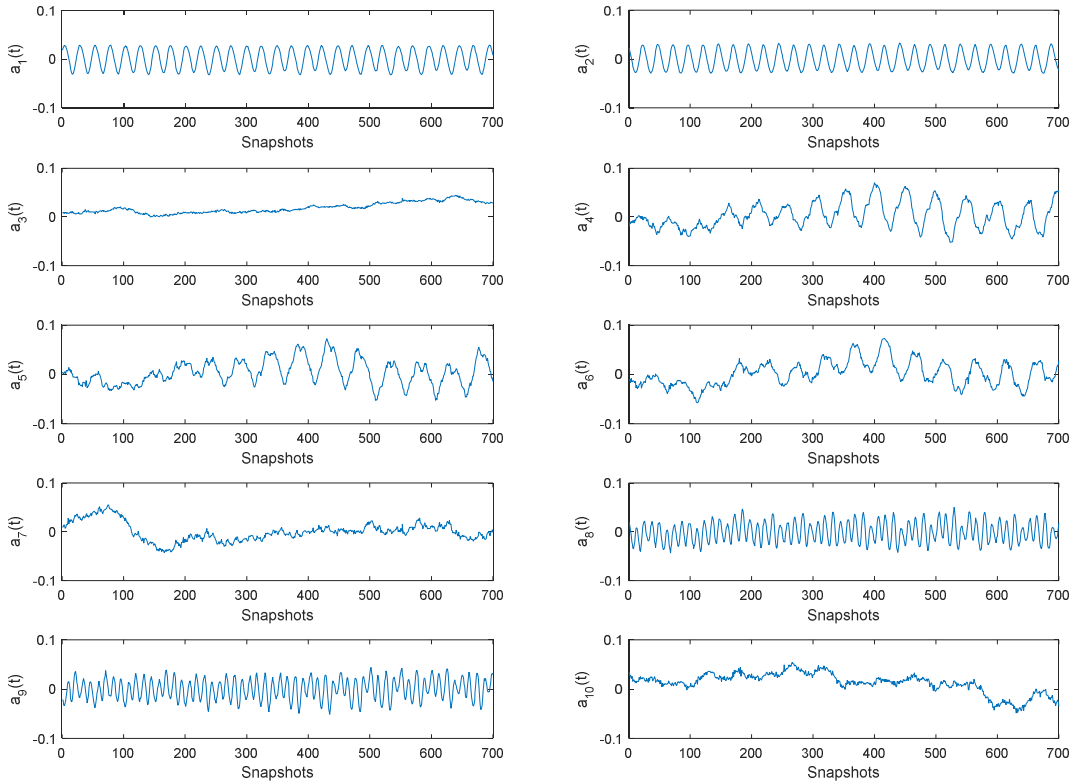


Figure 13: Temporal Evolution of the first ten modes  $a_n(t)$  for a POD 2D-2C

### 4.3 Reconstruction

In order to analyse the results of a reconstruction by taking into consideration the three velocity components, we visualised the results obtained by applying a Snapshot POD to the total kinematic field. Generally, the instantaneous velocity vector  $U(X, t)$  is acquired at time  $t_i$  where  $i = 1, 2, \dots, N$ . As already mentioned, the instantaneous kinematic fields are considered as snapshots of the flow field. For the reconstruction, a Snapshot POD was applied to the total kinematic field and on the 2500 snapshots of plane data. The three velocity components  $u, v, w$  of the SPIV data were arranged in the velocity matrix  $U$  such that:

$$U = [u^1 \quad u^2 \quad u^3 \dots \quad u^N]. \quad (10)$$

where  $u^i = [u_1^i \quad \dots \quad u_M^i \quad v_1^i \quad \dots \quad v_M^i \quad w_1^i \quad \dots \quad w_M^i]$ ,

with  $M$  = total number of grid points of the SPIV measurement plane. Thus, we defined the auto covariance matrix as:  $R = U^T U$ .

As explained in Section 3, the Eigen values are arranged in descending order, which means that the most important modes in terms of energy are the first modes. Therefore, if a flow has a dominant structure, the snapshots can be reconstructed by using only the first modes, which represent the dominant structure.

The linear combination of the Eigen vectors  $A$  and the instantaneous velocity vector  $U$  defines the POD modes or POD Eigen functions  $\phi^k$  as follows:

$$\phi^k(X) = \sum_{i=1}^N a_k(t_i) U(X, t_i), \quad k = 1, 2, \dots, N_{POD}. \quad (11)$$

From this decomposition, the reconstructed instantaneous velocity field  $u(x, t)$  is then deduced as follows:

$$u(X, t_i) = \sum_{k=1}^{N_{POD}} a_k(t_i) \phi^k(X), \quad i = 1, 2, \dots, N. \quad (12)$$

Generally, the POD technique is used to provide an optimal basis in the sense of energy. So, a discussion should be had about the number of modes to be considered that ensure a sufficient amount of energy that reflects the phenomena of the flow. Let the truncation order be  $K$ . By denoting  $N_{POD}$  the number of POD modes obtained by solving the Fredholm equation, the truncation error  $\varepsilon(K)$  to the order  $K$  is represented as follows:

$$\varepsilon(K) = \left\| u(X, t) - \sum_{n=1}^K [u(X, t), \phi^n(X)] \phi^n(X) \right\|^2 = \left\| \sum_{n=K+1}^{N_{POD}} [u(X, t), \phi^n(X)] \phi^n(X) \right\|^2. \quad (13)$$

Several definitions of the optimal dimension of the basis have been proposed, as explained by Podvin [37]. Sirovich [23] proposed a usable definition in which the sum of the energies of the modes represents at least 90% of the total energy and each of the neglected modes does not represent more than 1% of the main mode.

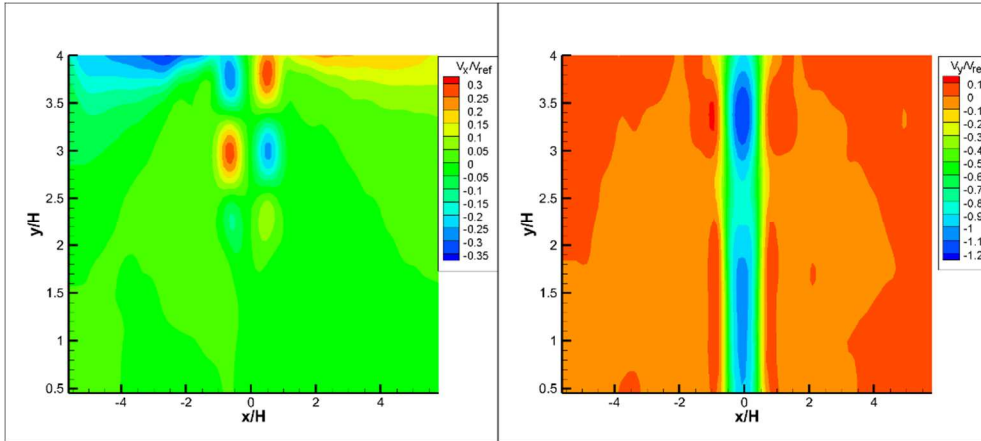


Figure 14: Reconstructed Kinematic Field by POD 2D-3C

We started by applying snapshot POD to one transversal plane  $P_0$ . The correlation tensor was constructed with three velocity components for the instantaneous velocity fields. The figure above (Figure 14) shows the results obtained by reconstructing the flow with three modes. The first 3 modes represent a cumulative energy of 95.83%. As mentioned before, the aim of this study was to reconstruct the flow with the least amount of information. As POD is a reduced order modelling, we chose to use snapshot POD with the instantaneous velocity field. The question remains concerning the dimension of the POD basis to be taken into consideration. As can be seen below in Figure 15, the reconstruction error between  $U$  and reconstructed

$U$  with three modes was on average 21.14%, which is an acceptable level. Note that the relative error obtained using the norm  $L_2$  was calculated as follows:

$$E_r(t) = \frac{\|U_{measured}(t) - U_{reconstructed}(t)\|_{L_2}}{\|U_{measured}(t)\|_{L_2}} = \frac{\sqrt{\sum_{i=1}^{10812} (U_{measured}(X_i, t) - U_{reconstructed}(X_i, t))^2}}{\sqrt{\sum_{i=1}^{10812} (U_{measured}(X_i, t))^2}}$$

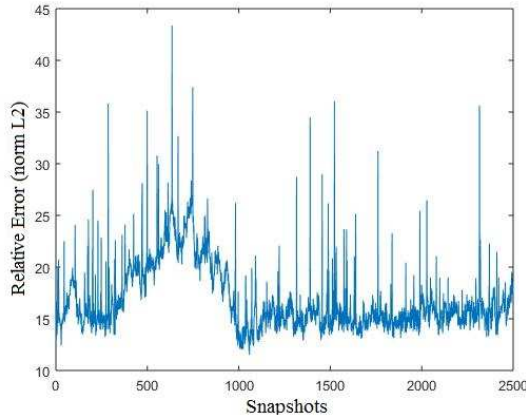


Figure 15: Reconstruction error (3 components - 3 modes)

## 5. Conclusion

The objective of the present work was to study the effect of the third component of the velocity field in the analysis of a jet. Two PIV campaigns were performed, the first using 2D-2C PIV acquisitions and the second using 2D-3C acquisitions. The results gave access to a three component velocity vector field and a snapshot POD was applied to the measured planes.

Three main results were compared to identify the effect of the third velocity component. First, the spatial POD modes were compared and we found that the first two modes were identical in both approaches (POD 2D-2C and POD 2D-3C). The third POD mode reflected the shear on the plate in both approaches. By considering the third velocity component, mode 4 showed the small structures on the plate, while for POD 2D-2C, modes which were greater than 4 reflected the small structures on the jet axis which were created between the large scale structures. Apart from mode 4, the rest of the modes were similar in both decompositions. The change over time of the coefficients of these spatial modes led to the same conclusions. Modes 1 and 2 representing the phenomenon of vortex passage were quasi-sinusoidal for both decompositions, showing that for large-scale structures the third component did not have much impact on the results. It should be noted that the comparison between a 2C and a 3C decomposition of the kinetic energy delivered by the Eigen values was remarkable. The energy convergence was much slower when considering the third velocity component where, to obtain 90% of the total kinetic energy only 61 modes were needed with POD 2D-2C, while 198 modes were needed for POD 2D-3C.

This paper was based on analysing the plane jet impinging on a slotted plate for a Reynolds number corresponding to 4458 and the effect of the third velocity component on large scale vortices. The next step will be to examine the turbulent kinetic energy of the flow, especially by using measurements of the 3C PIV results. In addition, the volume reconstruction of the fluctuating flow with POD and SPIV is another avenue that we would like to explore. All of these techniques will be tested with other Reynolds number and other confinements.

## 6. References

- [1] M.E. Hassan, H.H. Assoum, V. Sobolik, J. Vétel, K. Abed-Meraim, A. Garon, A. Sakout, Experimental investigation of the wall shear stress and the vortex dynamics in a circular impinging jet, *Exp. Fluids*. 52 (2012) 1475–1489. doi:10.1007/s00348-012-1269-5.

- [2] M.E. Hassan, H.H. Assoum, R. Martinuzzi, V. Sobolik, K. Abed-Meraim, A. Sakout, Experimental investigation of the wall shear stress in a circular impinging jet, *Phys. Fluids* 1994-Present. 25 (2013) 077101. doi:10.1063/1.4811172.
- [3] H. Martin, Heat and Mass Transfer between Impinging Gas Jets and Solid Surfaces, in: J.P. Hartnett, T.F. Irvine (Eds.), *Adv. Heat Transf.*, Elsevier, 1977: pp. 1–60. doi:10.1016/S0065-2717(08)70221-1.
- [4] B.W. Webb, C.-F. Ma, Single-Phase Liquid Jet Impingement Heat Transfer, in: J.P. Hartnett, T.F. Irvine (Eds.), *Adv. Heat Transf.*, Elsevier, 1995: pp. 105–217. doi:10.1016/S0065-2717(08)70296-X.
- [5] E. Forthmann, United States, National Advisory Committee for Aeronautics, Turbulent jet expansion, National Advisory Committee for Aeronautics, Washington, D.C., 1936.
- [6] S. Corrsin, Investigation of flow in an axially symmetrical heated jet of air., Calif. Inst. Technol.-NACA. (n.d.).
- [7] N. Rajaratnam, *Turbulent Jets*, Volume 5 - 1st Edition, (n.d.).  
[https://www.elsevier.com/books/turbulent-jets/rajaratnam/978-0-444-41372-7?start\\_rank=1&producttype=books&sortby=sortByRelevance&q=turbulent%20jets](https://www.elsevier.com/books/turbulent-jets/rajaratnam/978-0-444-41372-7?start_rank=1&producttype=books&sortby=sortByRelevance&q=turbulent%20jets) (accessed September 4, 2017).
- [8] I. Wygnanski, H. Fiedler, Some measurements in the self-preserving jet, *J. Fluid Mech.* 38 (1969) 577–612. doi:10.1017/S0022112069000358.
- [9] A. Billon, V. Valeau, A. Sakout, Two feedback paths for a jet-slot oscillator, *J. Fluids Struct.* 21 (2005) 121–132. doi:10.1016/j.jfluidstructs.2005.07.008.
- [10] A. Billon, V. Valeau, A. Sakout, Instabilités de l'écoulement produisant le bruit de fente, *Comptes Rendus Mécanique*. 332 (2004) 557–563. doi:10.1016/j.crme.2004.02.022.
- [11] M. Glessler, V. Valeau, A. Sakout, Vortex sound in unconfined flows: Application to the coupling of a jet-slot oscillator with a resonator, *J. Sound Vib.* 314 (2008) 635–649. doi:10.1016/j.jsv.2008.01.012.
- [12] H.H. Assoum, A. Sakout, M. El Hassan, J. Vetel, A. Alia, K. Abed-Meraïm, Experimental investigation of the vibration of a slotted plate and the acoustic field in a plane impinging jet, in: S.F. d'Acoustique (Ed.), *Acoust. 2012*, Nantes, France, 2012. <https://hal.archives-ouvertes.fr/hal-00810574> (accessed November 3, 2016).
- [13] H.H. Assoum, M. El Hassan, K. Abed-Meraim, A. Sakout, The vortex dynamics and the self sustained tones in a plane jet impinging on a slotted plate, *Eur. J. Mech. - BFluids*. 48 (2014) 231–235. doi:10.1016/j.euromechflu.2014.06.008.
- [14] H.H. Assoum, M.E. Hassan, K. Abed-Meraïm, R. Martinuzzi, A. Sakout, Experimental analysis of the aero-acoustic coupling in a plane impinging jet on a slotted plate, *Fluid Dyn. Res.* 45 (2013) 045503. doi:10.1088/0169-5983/45/4/045503.
- [15] H.H. Assoum, J. Hamdi, K. Abed-Meraïm, M. El Hassan, A. Hammoud, A. Sakout, Experimental investigation the turbulent kinetic energy and the acoustic field in a rectangular jet impinging a slotted plate, *Energy Procedia*. 139 (2017) 398–403. doi:10.1016/j.egypro.2017.11.228.
- [16] H.H. Assoum, J. Hamdi, K. Abed-Meraïm, M. El Hassan, M. Ali, A. Sakout, Correlation between the acoustic field and the transverse velocity in a plane impinging jet in the presence of self-sustaining tones, *Energy Procedia*. 139 (2017) 391–397. doi:10.1016/j.egypro.2017.11.227.
- [17] J. Hamdi, H. Assoum, K. Abed-Meraïm, A. Sakout, Volume reconstruction of an impinging jet obtained from stereoscopic-PIV data using POD, *Eur. J. Mech. - BFluids*. (2017). doi:10.1016/j.euromechflu.2017.09.001.
- [18] J. Hamdi, H.H. Assoum, K. Abed-Meraïm, A. Sakout, Volume reconstruction of a plane jet impinging on a slotted plate using the phase averaging technique, *Energy Procedia*. 139 (2017) 404–409. doi:10.1016/j.egypro.2017.11.229.
- [19] J.L. Lumley, The structure of inhomogeneous turbulent flows, *Atmospheric Turbul. Radio Wave Propag.* (1967) 166–178.
- [20] L. Grinberg, A. Yakhot, G.E. Karniadakis, Analyzing Transient Turbulence in a Stenosed Carotid Artery by Proper Orthogonal Decomposition, *Ann. Biomed. Eng.* 37 (2009) 2200–2217. doi:10.1007/s10439-009-9769-z.
- [21] S. Kefayati, T.L. Poepping, Transitional flow analysis in the carotid artery bifurcation by proper orthogonal decomposition and particle image velocimetry, *Med. Eng. Phys.* 35 (2013) 898–909. doi:10.1016/j.medengphy.2012.08.020.

- [22] G Berkooz, P Holmes, and J.L. Lumley, The Proper Orthogonal Decomposition in the Analysis of Turbulent Flows, *Annu. Rev. Fluid Mech.* 25 (1993) 539–575. doi:10.1146/annurev.fl.25.010193.002543.
- [23] L. Sirovich, Turbulence and Dynamics of Coherent Structures Part I: Coherent Structures, *Q. Appl. Math.* 45 (1987) 561–571.
- [24] S. Herzog, The large scale structure in the near-wall region of turbulent pipe flow, Cornell University, Jan., 1986.
- [25] J.P. Bonnet, D.R. Cole, J. Delville, M.N. Glauser, L.S. Ukeiley, Stochastic estimation and proper orthogonal decomposition: Complementary techniques for identifying structure, *Exp. Fluids.* 17 (1994) 307–314. doi:10.1007/BF01874409.
- [26] B.R. Noack, K. Afanasiev, M. Morzyński, G. Tadmor, F. Thiele, A hierarchy of low-dimensional models for the transient and post-transient cylinder wake, *J. Fluid Mech.* 497 (2003) 335–363. doi:10.1017/S0022112003006694.
- [27] J. Delville, Characterization of the organization in shear layers via the Proper Orthogonal Decomposition, *Appl. Sci. Res.* 53 (1994) 263–281. doi:10.1007/BF00849104.
- [28] B.R. Noack, M. Schlegel, B. Ahlborn, G. Mutschke, M. Morzyński, P. Comte, A Finite-Time Thermodynamics of Unsteady Fluid Flows, *J. Non-Equilib. Thermodyn.* 33 (2008) 103–148. doi:10.1515/JNETDY.2008.006.
- [29] N. Aubry, On The Hidden Beauty of the Proper Orthogonal Decomposition, in: *Stud. Turbul.*, Springer, New York, NY, 1992: pp. 264–265. doi:10.1007/978-1-4612-2792-2\_19.
- [30] P. Hémon, F. Santi, Simulation of a spatially correlated turbulent velocity field using biorthogonal decomposition, *J. Wind Eng. Ind. Aerodyn.* 95 (2007) 21–29. doi:10.1016/j.jweia.2006.04.003.
- [31] P. Schmid, Dynamic mode decomposition of numerical and experimental data, *J. Fluid Mech.* 656 (2010) 5–28. doi:10.1017/s0022112010001217.
- [32] A. Lasota, *Chaos, Fractals, and Noise - Stochastic Aspects of Dynamics* | | Springer, n.d. <http://www.springer.com/cn/book/9780387940496> (accessed October 15, 2017).
- [33] I. Mezić, Spectral Properties of Dynamical Systems, Model Reduction and Decompositions, *Nonlinear Dyn.* 41 (2005) 309–325. doi:10.1007/s11071-005-2824-x.
- [34] C.W. Rowley, I. Mezić, S. Bagheri, P. Schlatter, D.S. Henningson, Spectral analysis of nonlinear flows, *J. Fluid Mech.* 641 (2009) 115–127. doi:10.1017/S0022112009992059.
- [35] J. Hamdi, H. Assoum, K. Abed-Meraïm, A. Sakout, Proper Orthogonal Decomposition Analysis of a Confined Jet Impinging on a Slotted Plate, *Exp. Therm. Fluid Sci.* (Submitted).
- [36] A.K. Prasad, R.J. Adrian, C.C. Landreth, P.W. Offutt, Effect of resolution on the speed and accuracy of particle image velocimetry interrogation, *Exp. Fluids.* 13 (n.d.) 105–116. doi:10.1007/BF00218156.
- [37] B. Podvin, Y. Fraigneau, F. Lusseyran, P. Gougat, A Reconstruction Method for the Flow Past an Open Cavity, *J. Fluids Eng.* 128 (2005) 531–540. doi:10.1115/1.2175159.